CHEMPHYSCHEM

Supporting Information

Probing the Mechanical Properties of Hybrid Inorganic–Organic Frameworks: A Computational and Experimental Study

Monica Kosa,*[a] Jin-Chong Tan,[b] Crystal A. Merrill,[b] Matthias Krack,[c] Anthony K. Cheetham,*[b] and Michele Parrinello[a]

cphc_201000362_sm_miscellaneous_information.pdf

Contents

1. Hydrothermal Synthesis

A mixture of ZnO, Fisher Scientific, (2 mmol) and phosphonoacetic acid, Aldrich, (2 mmol) in 7.50 mL of deionized (DI) water was placed into an autoclave. The autoclave was then sealed and heated for 7 days at 200 °C (initial and final pH are 3.5 and 3, respectively). White powder containing colorless rod-shaped crystals suitable for structure determination and face-indexing were obtained.

2. Single-Crystal X-ray Diffraction

A suitable single-crystal (0.23 × 0.05 × 0.02 mm colorless rod) was selected under the polarizing microscope and attached to a thin glass fiber with microscope immersion oil (which froze upon mounting into the diffractometer). The diffraction experiment was performed on a Bruker-Nonius Kappa CCD diffractometer using a APEX II CCD camera and equipped with a Bruker-Nonius FR591 rotating anode X-ray source (Mo Ka radiation, ? = 0.71073 Å) operating at 50 kV and 85 mA. Data were collected at 120 K. A multi-scan absorption correction was applied using the SADABS[1] program. The structure was solved using direct methods implemented in the SHELXTL[2] package of programs, in which full-matrix least-squares refinement against $|F^2|$ was carried out. The hydrogen atoms were found in the Fourier difference map. The last cycles of refinement included atomic positions and anisotropic thermal parameters for all of the atoms except hydrogen, which used isotropic thermal parameters. The bond valence sums determined using the program VALIST[3,4] confirm the assignment of Zn as divalent. The program PLATON[5,6] was also used to verify the space group setting.

For face-indexing, a representative single crystal of 0.33 × 0.07 × 0.03 mm of **1** was selected and attached to a thin nylon loop with microscope immersion oil. Data was collected at 120 K on an Oxford Diffraction SuperNova using an Atlas CCD camera and equipped with a microfocus X-ray source (Cu Ka radiation, ? = 1.5418 Å) operating at 50 kV and 1 mA. The unit cell was indexed from 68 reflections and the faces were defined using the face-indexing module in CrysAlis^{Pro} software.

Table S1. Crystal data and structure refinement parameters for **1**.[7]

Empirical formula	$Zn_3(H_2O)(PO_4)(O_2CCH_2PO_3)$
Formula weight	446.10
Crystal system	Triclinic
Space group	$P\,\bar{1}$ (No. 2)
a /Å	4.90930(10)
b /Å	9.5271(2)
c /Å	11.1246(3)
α /°	64.8130(10)
β /°	82.915(2)
γ /°	81.068(2)
V/Å^3	464.179(18)
Z	2
Density (calc) /g cm^{-3}	3.192
Absorption coefficient /mm^{-1}	8.079
F(000)	432
? range data collected	3.71 to 27.51
Total reflections	8660
Unique reflections	2117 [R_{int} = 0.0225]
Refinement Method	Full matrix least squares on $\|F^2\|$
Data/ restraints/ parameters	2117 / 2 / 168
R indexes [$I > 2\sigma(I)$]	R_1= 0.0217[a] ; wR_2 = 0.0537[b]
R indexes (all data)	R_1= 0.0207[a] ; wR_2 = 0.0530[b]
Goodness of fit (GOF)	1.092
Largest difference peak & hole	0.515 and –0.834 e · Å^{-3}

[a] $R_1 = \Sigma\,||F_0|-|F_c|| / \Sigma\,|F_0|$; [b] $wR_2 = \{\Sigma[w(F_0^2 - F_c^2)^2] / \Sigma[w(F_0^2)^2]\}^{1/2}$. $w = 1/[\sigma^2(F_0)^2 + (aP)^2 + bP]$, $P = [\max.(F_0^2,0) + 2(F_c)^2]/3$, where $a = 0.0127$ and $b = 1.6039$

3. Chemical Verification

3.1 Elemental analysis

Table S2. C, H, P elemental analysis of **1**

	Observed	Calculated
wt% C	5.86	5.38
wt% H	0.92	0.90
wt% P	13.76	13.88

3.2 Fourier transform infra-red spectroscopy

FTIR measurements were carried out on a Bruker Optics Tensor 27 ATR-FT-IR Spectrometer. FTIR frequencies for **1** above 1400 cm^{-1}: 1585 s, 1420 m.

3.3 Thermal analysis

Thermogravimetric analyses of **1** were carried out with a heating rate of 5 °C min^{-1} in air on a TA Instruments TGA Q500. Variable temperature X-ray diffraction (Cu Ka radiation, ? = 1.5418 Å) was performed under static air in a Bruker D8 Advance diffractometer outfitted with a LynxEye position-sensitive detector and an Anton Paar HTK 16 high-temperature stage. Patterns were scanned at 30 °C, 100 °C, and every 50 °C thereafter until 650 °C, with a temperature ramp of 1 °C min^{-1}.

1 is stable to ~265 °C, at which point it begins to lose coordinated water and a structural change begins (Figure S1). These changes are complete by 400 °C. The dehydrated phase is stable to 450 °C, at which point the structure begins to evolve some organics and transform into $Zn_3(PO_4)_2$. The sample fraction of $Zn_3(PO_4)_2$ grows and the remaining organic is removed from the structure between 500 °C and 750 °C.

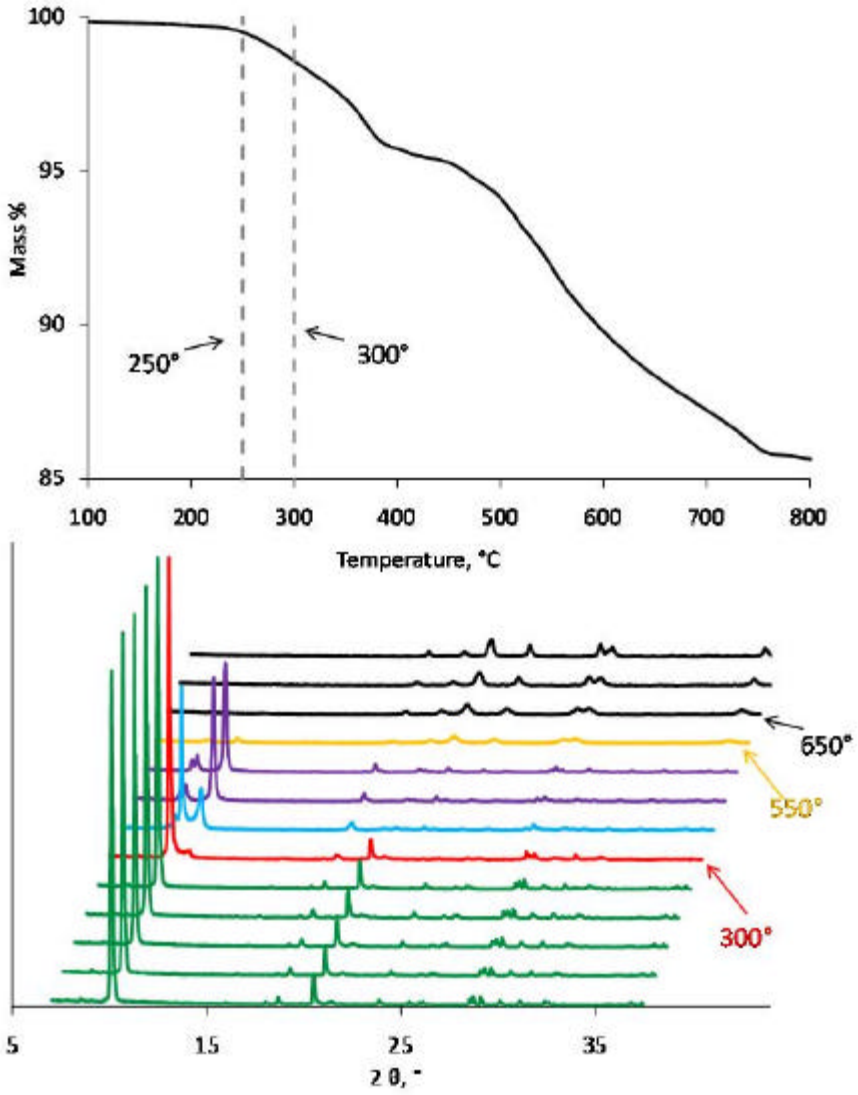

Figure S1. TGA curve (top) and thermo-diffraction pattern in air at room temperature, 100 °C and every 50 °C until 650 °C (bottom) of **1.**

4. DFT Studies

4.1 Density functional theory calculations

For geometry and cell optimizations, all structures reported here were calculated using the PBE[8] functional, GTH[9] pseudopotential with the TZV2P[10] Gaussian basis set and 700 Ry plane wave density cutoff as implemented in the QS module[11] of the CP2K package.[12] The convergence of the total energy with respect to the plane wave basis set was checked in the range of 300−1800 Ry, with intervals of 100 Ry (see SI). The relatively high and safe value of 700 Ry was chosen in order to avoid inconsistencies due to different cell sizes with respect to the plane wave basis set. For hydrostatic pressures, the stresses were relaxed via geometry optimizations up to a tolerance of 1% of the applied pressure (for the diagonal elements of the stress tensor).

4.2 Convergence of total energy with respect to cutoff, relative cutoff and Gaussian basis sets

The geometry and cell parameters of the orthorhombic 168 atoms structure were optimized at the cutoff/relative cutoff[13] of 400/30. Single point energy calculations, at relative cutoff of 30 in the range of 300−1800 were performed. The data set is shown in Figure S2.

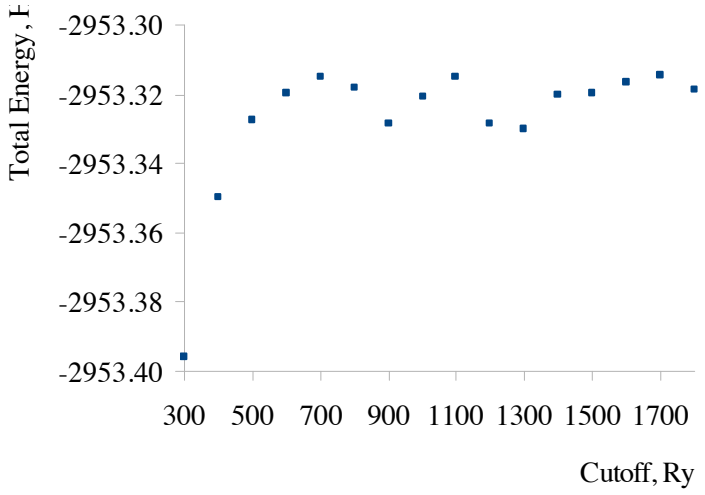

Figure S2. Total energy (in Hartree) as a function of plane wave density cutoff.

To check the convergence of the total energy with respect to the relative cutoff, single point energy calculations were performed at varying values of both parameters, the data set is shown in Figure S3.

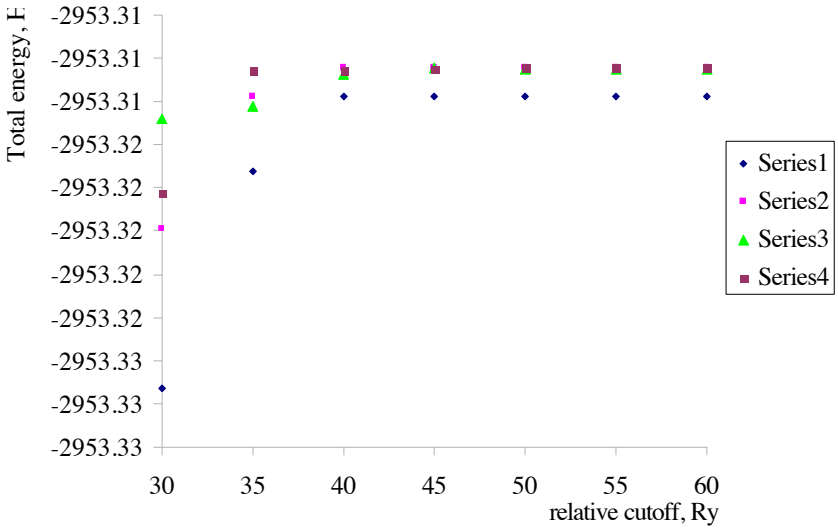

Figure S3. Total energy as function of relative cutoff for several cutoff values (in Ry): blue 500, pink 600, green 700, maroon 800.

For hydrostatic pressure studies of the orthorhombic cell, the optimized cell parameters corresponding to pressure 1±1 bar are: a = 10.120 Å , b = 9.551 Å, c = 20.610 Å, a = 89.627° , β = 84.989°, γ = 87.204°.

4.3 Band gaps (eV) of 1 and ZnO.

	1	ZnO
PADE+U, U_{eff}=0 eV	3.61	0.56
PADE+U, U_{eff}=5 eV	3.77	1.11
PADE+U, U_{eff}=7 eV	3.82	1.25
PADE+U, U_{eff}=10 eV	3.88	1.41
PBE	3.88	0.73
PBE+U, U_{eff}= 5 eV	4.09	
PBE+U, U_{eff}= 7 eV	4.10	
PBE+U, U_{eff}= 10 eV	4.15	
PBE0	6.32	2.71
Experimental	5.41	3.27

Table S3. Calculated geometrical parameters employing different Gaussian basis sets, with BLYP and PBE functionals, according to designation in Scheme 1.

	Experimental	Cell parameters **not** optimized Geometry optimized			Cell parameters optimized and geometry optimized		
		BLYP/GTH-TZVP(H, C, O, P) TZV(Zn)	PBE/GTH-TZVP(H, C, O, P) TZV(Zn)	PBE/GTH-TZV2P(H, C, O, P) TZV(Zn)	PBE/GTH-TZVP(H, C, O, P) TZV(Zn)	BLYP/GTH-TZVP(H, C, O, P) TZV(Zn)	BLYP/GTH-TZVP(H, C, O, P) TZV(Zn)
	With water	With water	With water	With water	With water	With water	Without water
orthorhombic cell parameters	-	9.988 9.4120 20.0930	9.9880 9.4120 20.0930	9.9880 9.4120 20.0930	10.281 9.671 20.506	10.104 9.712 20.470	10.341 9.844 20.731
Zn - bipyramid							
r_1	2.31	2.45	2.52	2.41	2.35	2.38	2.21
r_2	1.91	1.94	1.95	1.94	1.94	1.96	1.97
r_3	1.94	1.93	1.93	1.92	1.96	1.98	1.99
r_4	2.24	2.25	2.18	2.28	2.21	2.20	2.12
r_5	1.96	1.99	1.99	2.00	2.01	2.03	-
$?_1$	114.2	119.3	119.3	118.5	123.5	120.3	131.2
$?_2$	174.9	177.0	176.6	177.8	167.2	167.9	157.5
Zn - tetrahedral							
r_1	1.99	2.08	2.06	2.06	2.05	2.05	2.09
r_2	1.97	2.01	2.00	2.00	2.01	2.03	2.01
r_3	1.94	1.94	1.95	1.95	1.95	1.97	1.96
r_4	1.89	2.00	2.00	2.02	1.99	2.01	1.97
Zn - octahedral							
r_1	2.13	2.04	2.01	2.03	2.07	2.11	2.07
r_2	2.14	2.25	2.27	2.29	2.62	2.63	2.23
r_3	2.09	2.02	2.00	2.01	2.03	2.05	2.13
r_4	2.06	2.03	2.02	2.04	2.09	2.18	2.08
r_5	2.15	2.26	2.26	2.27	2.32	2.38	2.72
r_6	2.19	2.46	2.41	2.38	2.13	2.11	2.19

C-C	1.50	1.50	1.49	1.5	1.51	1.51	1.51
C-P	1.81	1.85	1.84	1.84	1.85	1.85	1.86
PO_4	1.51, 1.51, 1.54, 1.56	1.57, 1.57, 1.59, 1.61	1.57, 1.57, 1.59, 1.61	1.55, 1.56, 1.56, 1.59	1.57, 1.58, 1.59, 1.61	1.58, 1.58, 1.60, 1.62	1.57, 1.59, 1.60, 1.61

Scheme1. Geometrical parameter designation.

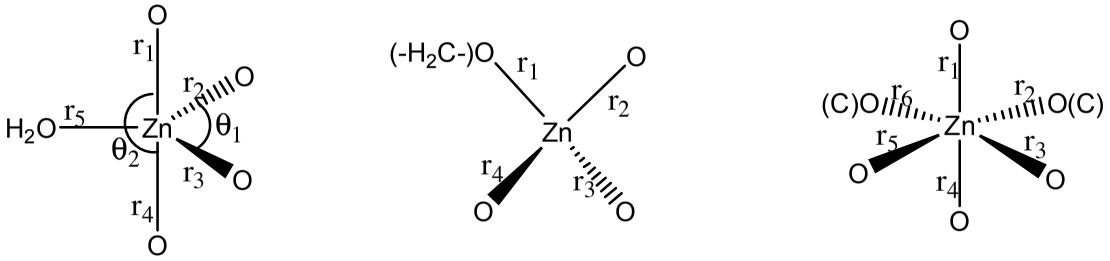

4.4 Bulk modulus calculation

Absolute and relative cell parameters of **1t-s** and **1t-l** upon application of hydrostatic pressures in the range of 0–5 GPa.

Table S4. **1t-s**

Internal pressure, GPa	Volume, Å^3	x	x/x_o	y	y/y_o	z	z/z_o
0.0	1969.34	10.024	1.000	9.709	1.000	22.786	1.000
0.5	1951.252	10.000	0.998	9.669	0.996	22.723	0.997
1.0	1929.147	9.969	0.995	9.618	0.991	22.644	0.994
2.0	1889.086	9.919	0.990	9.517	0.980	22.45	0.985
3.0	1851.927	9.862	0.984	9.442	0.972	22.19	0.974
4.0	1816.276	9.805	0.978	9.337	0.962	22.004	0.966
5.0	1779.348	9.731	0.971	9.272	0.955	21.729	0.954

Table S5. **1t-l**

Internal pressure, GPa	Volume, Å^3	x	x/x_o	y	y/y_o	z	z/z_o
0.0	2951.542	15.018	1.000	9.71	1.000	22.771	1.000
1.0	2881.102	14.941	0.995	9.611	0.990	22.473	0.987
2.0	2825.493	14.86	0.989	9.517	0.980	22.314	0.980
3.0	2772.94	14.783	0.984	9.428	0.971	22.124	0.972
4.0	2726.363	14.689	0.978	9.362	0.964	21.983	0.965
5.0	2671.644	14.616	0.973	9.266	0.954	21.744	0.955

The calculated data on the compressibility of the smaller (1t-s) and the larger (1t-l) simulation cells suggests that the electronic structure is already converged within the smaller, 1t-s, simulation cell (only Γ-point for Brillouin zone integration). This simulation cell was subsequently used in finite strain calculations.

Table S6. **1t-s** Bulk modulus calculations: $B = -V_0(dP/dV)$

Internal pressure, GPa	Volume, Å^3	Linearized volume	B, GPa, Vol. lin.	B, GPa
0.0	1969.34	1967.998	51.5548	
0.5	1951.252	1948.947	51.5592	54.3431
1.0	1929.147	1929.981	51.5570	48.7997
2.0	1889.086	1892.337	51.5559	48.6385
3.0	1851.927	1854.296	51.5555	49.9603
4.0	1816.276	1815.214	51.5553	51.4961
5.0	1779.348	1777.525	51.5552	51.7209

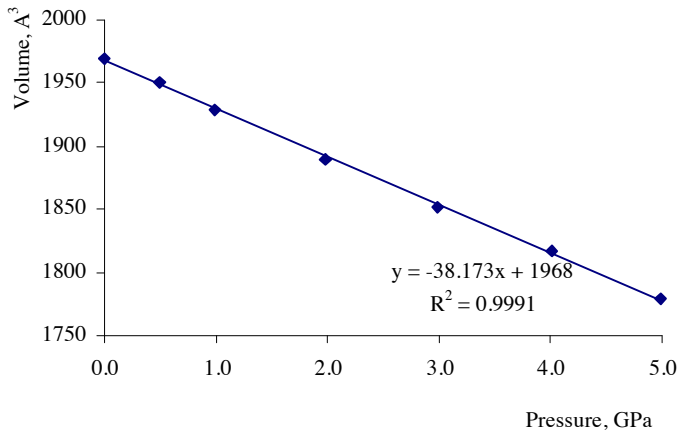

Figure S6. Calculated *P*- *V* relationship for the 1t-s model

4.5 General considerations for bulk modulus (*B*) calculation of anisotropic materials

All MOFs investigated so far from the IRMOF family, are assumed to be isotropic and their elastic properties were studied by fitting the energy volume data to a quadratic equation of state, derived from isotropic alternations of the cell parameters, and subsequent relaxation of atomic coordinates in those predefined cells (either by 0 K geometry minimizations or molecular dynamics sampling). Such methodology can become unreliable when the structure has elastic anisotropy. Astala *et al.*[14] have demonstrated that for anisotropic silica zeolite compounds, fixed volume calculations can lead to overestimation of the bulk modulus by ~26%, in the case of silica mordenite. To remedy this, the authors have calculated elastic tensor components by varying lattice parameters and fitting the total energy versus lattice parameter to a quadratic polynomial. Available elastic tensor components, C_{ij}, were combined to extract the bulk modulus, B, according to $B = (\Sigma(C^{-1})_{ij})^{-1}$. It was noted in the same work that using symmetry in such calculations can lead to spurious results due to the inability of the calculated compound to collapse to a lower symmetry structure upon cell deformation. As an alternative to the traditional approach (for isotropic materials) for the calculation of the bulk modulus where the volume is changed isotropically in all directions, for highly anisotropic materials, Kim *et al.*[15] proposed to consider the uniaxial compression which leads to a decrease in volume. This approach however requires prior knowledge of directional mechanical properties of the material, either from experiment or preliminary computations. As such, the approach of Kim cannot be used for general anisotropic materials – where uniaxial compression of the volume cannot serve as a valid approximation to the compression induced by hydrostatic pressure.

4.6 Approximated Young's modulus (*E*) derivation scheme

The general theory of elasticity states that in the case of unconstrained compression (or tension), application of a unidirectional stress (i.e., force per unit area), for example in the *x*-direction (σ_{xx}), will result in deformation of the material along that axis, i.e. strain ε_{xx}. Because of Poisson's effect, this also gives rise to strains in the *y*- and *z*-directions, i.e. ε_{yy} and ε_{zz} respectively. There are, however, no stresses accompanying these strains ($\sigma_{yy} = \sigma_{zz} = 0$) since the system is not restrained in the orthogonal axes. It follows that the stress-strain relationship of such a system is simply given by the Hooke's Law: $\varepsilon_{xx} = \sigma_{xx}/E_x$, where E_x is the Young's modulus along the *x*-axis.

In the case of constrained deformation, i.e. when the material is confined in such a way that upon application of forces in the *x*-direction, the stresses along the *y*- and *z*-directions are non zero, the strain ε_{xx} induced by σ_{xx} will be smaller due to imposed resistance along the *y*- and *z*-directions. This dependence can be approximated by the following stress-strain relationship (and becomes exact for an orthorhombic case):

$$\varepsilon_{xx} = \frac{\sigma_{xx}}{E_x} + (-\nu_{yx}) \cdot \frac{\sigma_{yy}}{E_y} + (-\nu_{zx}) \cdot \frac{\sigma_{zz}}{E_z} \tag{1}$$

where ν_{ij} is the Poisson's ratio, which is defined as the negative ratio of transverse strain to longitudinal strain, i.e. $-\varepsilon_j/\varepsilon_i$.

By analogy to *x*, for the *y*- and *z*-directions this expression takes the following forms for ε_{yy} and ε_{zz}, respectively:

$$\begin{aligned} \varepsilon_{yy} &= (-\nu_{xy}) \cdot \frac{\sigma_{xx}}{E_x} + \frac{\sigma_{yy}}{E_y} + (-\nu_{zy}) \cdot \frac{\sigma_{zz}}{E_z} \\ \varepsilon_{zz} &= (-\nu_{xz}) \cdot \frac{\sigma_{xx}}{E_x} + (-\nu_{yz}) \cdot \frac{\sigma_{yy}}{E_y} + \frac{\sigma_{zz}}{E_z} \end{aligned} \tag{2}$$

The above relationships can be recast in a matrix notation of the form $[\varepsilon] = [\sigma][x]$:

$$[\varepsilon] = \begin{pmatrix} \varepsilon_{xx} & 0 & 0 \\ 0 & \varepsilon_{yy} & 0 \\ 0 & 0 & \varepsilon_{zz} \end{pmatrix} \quad ; \quad [\sigma] = \begin{pmatrix} \sigma_{xx}^{x} & \sigma_{yy}^{x} & \sigma_{zz}^{x} \\ \sigma_{xx}^{y} & \sigma_{yy}^{y} & \sigma_{zz}^{y} \\ \sigma_{xx}^{z} & \sigma_{yy}^{z} & \sigma_{zz}^{z} \end{pmatrix} \quad ; \quad [x] = \begin{pmatrix} \frac{1}{E_x} & \frac{-\nu_{xy}}{E_x} & \frac{-\nu_{xz}}{E_x} \\ \frac{-\nu_{yx}}{E_y} & \frac{1}{E_y} & \frac{-\nu_{yz}}{E_y} \\ \frac{-\nu_{zx}}{E_z} & \frac{-\nu_{zy}}{E_z} & \frac{1}{E_z} \end{pmatrix} \tag{3}$$

The strained cell parameters of the triclinic cell **1** (h_mat_new) are obtained by deformation of the *h* matrix according to: h_mat_new = (*I*+ε)*h_mat, where the h_mat are the cell parameters geometrically optimized at 1 bar. Here, we are treating the crystallographic *a*-, *b*- and *c*-directions as the *x*-, *y*- and *z*-axes (hence the approximation).

To solve the system of equations in (3), the strains, ε_{ii}, are applied consecutively (while constraining other directions), the geometry is optimized and the corresponding stresses are calculated (at the optimized geometries). For example, for $\varepsilon_{ii} = \varepsilon_{xx}$ the calculated stresses are σ^{x}_{xx}, σ^{x}_{yy} and σ^{x}_{zz} (which are the diagonal elements of the full stress tensor). The system of equations is solved by varying the (compressive) strains from $\varepsilon_{ii} = 0.005$ to $\varepsilon_{ii} = 0.05$ (small strains to represent elastic regime), and by designating ε_{ii} as ε_{xx}, or ε_{yy}, or ε_{zz} for each solution. The resulting relative Young's moduli are shown in Figure S7.

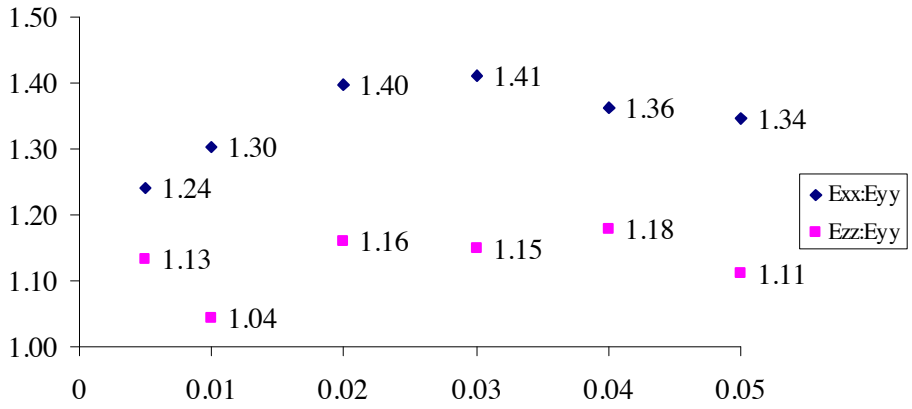

Figure S7. The calculated relative Young's moduli E_x:E_y (blue) and E_z:E_y (pink) as a function of strain.

4.7 Summary of reported elastic properties of ZnO

Table S7. The elastic constants C_{ij}, Young's modulus (E) and bulk modulus (B) of ZnO calculated by DFT, and experimental data obtained from Brillouin Zone (BZ) scattering.

Ref.	Code	DFT scheme	C_{11}/GPa	C_{12}	C_{13}	C_{33}	C_{44}	$E\{100\}$*/GPa	$E\{001\}$	$E\{101\}$	B /GPa
Kalay (2009)[16]	VASP	PBE/PAW	235.025	66.742	60.95	287.891	49.891	209.1	263.3	147.7	129.19
Fan (2008)[17]	CASTEP	PBE/Vanderbilt	191.9	107.3	88.6	217.0	38.3	123.2	164.5	108.9	130.0
		LDA/Vanderbilt	231.7	138.3	113.1	256.4	40.9	138.8	187.3	118.6	161.0
Gopal (2006)[18]	VASP	LDA/(SIC-PP?)	217	117	121	225	50	134.2	137.3	135.8	-
Wrobel (2007)[19]	VASP	UPBE/PAW									131.370
											122.128
											127.630
											128.399
Saib (2007)[20]	ABINIT	LDA-PW	278	87	98	287	57	233.1	234.4	169.1	156.55
		GGA-PBE	227	55	93	206	49	184.1	144.7	141.9	126.73
Maouche (2007)[21]	CASTEP	LDA(?)									164.36
Amrani (2006)[22]	WIEN2K	LDA/MuffinTin +PW									168.4
Wang** (2006)[23]	ABINIT	LDA/	181.9	143.8	–	–	86.6	54.9	54.9	125.5	151.8
Yu (2006)[24]	CASTEP	GGA									132.02
		GGA									131.48
Serrano (2004)[25]	ABINIT	LDA(PZ)									159.5
Carlotti*** (1995)[26]	Exp.	BZ scattering	206	116.8	118	211	44.3	120.9	125.1	121.5	

* The Young's moduli along different crystallographic orientations, i.e. $E\{hkl\}$, were determined using relationships found in pg.145 of Ref.[27].
** Zinc blende structure (cubic).
*** Measured for the ZnO film. Similar values were reported for the bulk material, see reference 20 in Ref.[26] of this manuscript.

5. Nanoindentation Studies

Nanoindentation experiments were performed under ambient conditions using an MTS Nanoindenter XP, equipped with a Continuous Stiffness Measurement (CSM) module. 15 indents to a depth of 500 nm were made using a Berkovich (three-sided pyramidal) diamond tip, onto each of the (100)-, (010)- and (001)-oriented crystal facets (see Figure 2B in Manuscript). The loading and unloading strain rates were maintained at 0.05 s^{-1}. A 2-nm sinusoidal displacement at 45 Hz was superimposed onto the system primary loading signal, while the response was tracked through a frequency-specific amplifier. At the preset maximum displacement (h_{max}) of 500 nm, the indenter was held for 30 seconds prior to unloading (to minimize creep effects). Experiments were conducted under the CSM mode so that the Young's modulus (E) can be obtained as a function of the surface penetration depth (h).

The orientation of the crystal was established via single-crystal X-ray diffraction. The facet to be probed was first cold-mounted using an epoxy resin and then carefully polished using increasingly fine diamond suspensions to achieve a final surface roughness of less than 10 nm (rms value obtained by atomic force microscopy). The preparation of high quality sample surfaces is critical to minimize experimental uncertainty.

The nanoindenter calibration was performed using a fused silica standard, with elastic modulus (72 GPa) and hardness (9 GPa) that are of the same order of magnitude as the hybrid crystals being investigated here. Thermal drifts were ensured to be consistently low (typically less than 0.05 nm s^{-1}). In addition, the inter-indent spacing was ensured to be at least 50 times the indentation depth to avoid interaction of deformed zones (Figure 2A).

Under the dynamic nanoindentation mode, the change in the elastic contact stiffness (S) between the indenter tip and the sample surface was continuously monitored, from which the reduced modulus (E_r) is given by:[28]

$$E_r = \frac{\sqrt{\pi}}{2\beta}\frac{S}{\sqrt{A_c}} \tag{4}$$

where A_c is the contact area under load (predetermined from a calibrated tip areal function), and β is a constant that depends on the geometry of the indenter (β = 1.034 for a Berkovich tip).

Subsequently the method of Oliver and Pharr[29] can be used to extract E from the reduced modulus (E_r):

$$\frac{1}{E_r} = \left(\frac{1-\nu_s^2}{E}\right) + \left(\frac{1-\nu_i^2}{E_i}\right) \tag{5}$$

where E_i and ν_i are the elastic modulus and Poisson's ratio of the indenter, respectively (diamond tip: E_i = 1141 GPa and ν_i = 0.07), and ν_s is the sample Poisson's ratio. All elastic moduli presented in this work were determined by taking the sample Poisson's ratio to be approximately equal to 0.25, noting that ν_s is 0.18 for fused silica and ~0.28 for MOF-5.[30] We emphasize that the calculated value of E is in fact not particularly sensitive to the absolute value of ν_s. From Eqn. (5), one has that a 50% increase in ν_s from 0.2 to 0.3 results in only a 5% difference in the corresponding values of E.

References

[1] G. M. Sheldrick, SADABS - Siemens Area Detector Absorption Correction Program. University of Göttingen, Göttingen, Germany, 1994.

[2] G. M. Sheldrick, SHELXTL-PLUS Program for Crystal Structure Solution and Refinement. University of Göttingen, Göttingen, Germany, 1997.

[3] A. S. Wills, VaList - Bond Valence Calculation and Listing, University College London: London, United Kingdom, 1998-2008.

[4] N. E. Brese, M. O'Keefe, Acta Cryst. 1991, B47, 192-197.

[5] A. L. Spek, PLATON, A Multipurpose Crystallographic Tool, Utrecht University: Utrecht, The Netherlands, 2008.

[6] A. L. Spek, J. Appl. Cryst. 2003, 36, 7-13.

[7] CCDC 761446 contains the crystallographic data for this paper that can be obtained free of charge from the Cambridge Crystallographic Data Centre via www.ccdc.cam.ac.uk/data_request/cif

[8] J. P. Perdew, K. Burke, M. Ernzerhof, *Phys. Rev. Lett.* **1996**, *77*, 3865-3868.

[9] a) S. Goedecker, M. Teter, J. Hutter, *Phys. Rev. B* **1996**, *54*, 1703-1710; b) M. Krack, *Theor. Chem. Acc.* **2005**, *114*, 145-152.

[10] The accuracy of the TZVP Gaussian basis set with respect to structural data was validated for the model of **1** (see SI) and other systems as well (see ref. 11b).

[11] a) M. Krack, M. Parrinello, *Forschungszentrum Jülich, NIC Series* **2004**, *25*, 29; b) J. VandeVondele, M. Krack, F. Mohamed, M. Parrinello, T. Chassaing, J. Hutter, *Comp. Phys. Comm.* **2005**, *167*, 103-128.

[12] http://cp2k.berlios.de

[13] In Quickstep/CP2K, multigrids are used to compute matrix elements and densities. The accuracy of the multigrid method is defined by the plane wave cutoff of the grid used for Gaussians. 40 Ry was found to be accurate. (a) G. Lippert, J. Hutter, M. Parrinello, Theor. Chem. Acc. (1999), 103, 124. (b) J. VandeVondele, M. Krack, F. Mohamed, M. Parrinello, T. Chassaing, J. Hutter, *Comp. Phys. Comm.,* **2005**, *167*, 103.

[14] R. Astala, S. M. Auerbach, P. A. Monson, J. *Phys. Chem. B*, **2004**, *108*, 9208.

[15] E. Kim, C. Chen, *Phys. Lett. A*, **2004**, *326*, 442.

[16] M. Kalay, H. H. Kart, S. Ozdemir Kart, T. Cagin J. Alloys Comp., 2009, 484, 431–438.

[17] C. Fan, Q. Wang, L. Li, S. Zhang, Y. Zhu, X. Zhang, Appl. Phys. Lett., 2008, 92, 101917.

[18] P. Gopal, N. A. Spaldin, J. Electr. Mat., 2006, 35, 538.

[19] J. Wróbel, J. Piechota, Phys. Stat. Sol. 2007, 244, 1538–1543.

[20] S. Saib, N. Bouarissa, Phys. Stat. Sol. 2007, 244, 1063–1069.

[21] D. Maouche, F. Saad Saoud, L. Louail, Mat. Chem. Phys. 2007, 106, 11–15.

[22] B. Amrani, I. Chiboub, S. Hiadsi, T. Benmessabih, N. Hamdadou Sol. State Comm.2006, 137, 395–399.

[23] S. Q. Wang, J. Cryst. Growth, 2006, 287, 185–188.

[24] Z. Gen Yua, H. Gongb, P. Wua, J. Cryst. Growth, 2006, 287, 199–203.

[25] J. Serrano, A. H. Romero, F. J. Manjón, R. Lauck, M. Cardona, A. Rubio, Phys. Rev. B, 2004, 69, 094306.

[26] G. Carlotti, D. Fioretto, G. Socino, E. Verona, J. Phys.: Condens. Matter, 1995, *7,* 9147-9153.

[27] J. F. Nye, Physical Properties of Crystals: Their Representation by Tensors and Matrices. Oxford University Press Inc., New York, 1985.

[28] A.C. Fisher-Cripps, Nanoindentation, 2nd ed., Springer, New York, 2004.

[29] W. C. Oliver, G. M. Pharr, J. Mater. Res., 1992, 7, 1564-1583.

[30] D. F. Bahr, et al., Phys. Rev., 2007, B 76, 184106.